ACS Energy LETTERS

http://pubs.acs.org/journal/aelccp

Intermediate State Formation Extends the Ambient Temperature Processing Window of Solution-Processed Perovskite Solar Cells

Yunfan Wang,◆ Zhuoqiong Zhang,◆ Zixin Zeng, Yuxuan Zhang, Tianli Hu, Leyu Bi, Yajie Yang, Shanchao Ouyang, Xia Hao, Chenjie Xu, Yuanhang Cheng, Hanlin Hu, Alex K.-Y. Jen, Johnny C. Ho, Tom Wu,* and Sai Wing Tsang*

Cite This: *ACS Energy Lett.* 2025, 10, 647−657

Read Online

ACCESS | Metrics & More | Article Recommendations | Supporting Information

ABSTRACT: **Solution-processed perovskites offer tremendous potential for low-cost, high-throughput photovoltaic production. However, high-quality perovskite films typically require stringent processing conditions, compromising reliability in large-scale production. Here, we discover that the initial nucleation process during the spin-coating is critical in determining the film quality. This process is highly sensitive to ambient temperature (T_A) and associated with the effectiveness of intermediate phase formation. Besides the general wisdom that the intermediate phase regulates the initial nucleation by temporarily consuming precursor ions, we find that the intermediate phase plays a key role in guaranteeing high film quality by spatially separating the nuclei to mitigate thermally activated nuclei aggregation. By stabilizing a strongly coordinated intermediate phase, we achieve perovskite solar cells (PSCs) with power conversion efficiencies of 24% to 25%, even T_A elevated to 28 °C. This work offers valuable insights into enhancing the reliability of PSCs and provides a deeper understanding of the role of the intermediate phase in the solution-processing of perovskite films.**

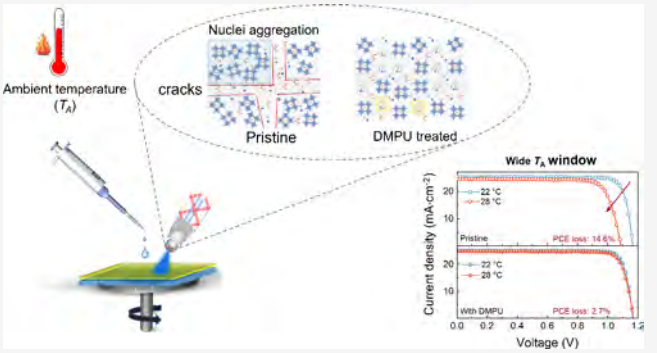

Metal−organic halide perovskite has become a crucial component in photovoltaic (PV) technology due to its excellent photoelectric properties. Since it was first reported in 2009, the power conversion efficiency (PCE) of perovskite solar cells (PSCs) has increased from 3.8% to 26.7%.[1−6] The ease of perovskite layer fabrication using simple solution methods demonstrates outstanding potential for low-cost and large-area PV module production.[7−10] Among various perovskite materials, formamidinium lead triiodide ($FAPbI_3$) perovskite has attracted tremendous attention for developing high-efficiency single junction PSCs due to its desirable bandgap (1.48 eV).[11,12] To date, high-efficiency FA-based PSCs are generally fabricated using the antisolvent-assisted one-step solution-processing method, which is a simple and efficient approach to achieve dense and highly crystalline perovskite thin films.[13−15] In a pioneer work by Jeon and co-workers in 2014, a mixed solvent of γ-butyrolactone and dimethyl sulfoxide (DMSO) followed by toluene drop-casting was used to produce uniform and dense perovskite layers significantly improved the PCE of PSCs to 16.2%.[2] Since then, the one-step method has become a general practice to fabricate the perovskite films. In a recent work, using the same approach, Chen et al. have achieved a record-high PCE of 26.91% in a small area (0.049 cm^2) PSC device.[16]

However, it is well-known that the quality of perovskite films is very sensitive to the fabrication conditions, such as solvent and antisolvent, additive, ambient humidity, and temperature, etc.[17−20] Therefore, the reproducibility of PSCs based on a one-step method remains challenging, which hinders the deployment for large-scale production in commercialization. Besides the precise control of antisolvent dripping time, an inert gas or dry air atmosphere with strictly controlled ambient temperatures is found critical to ensure the perovskite film quality during the fabrication process. It is widely recognized

Received: November 11, 2024
Revised: December 15, 2024
Accepted: December 23, 2024
Published: January 6, 2025

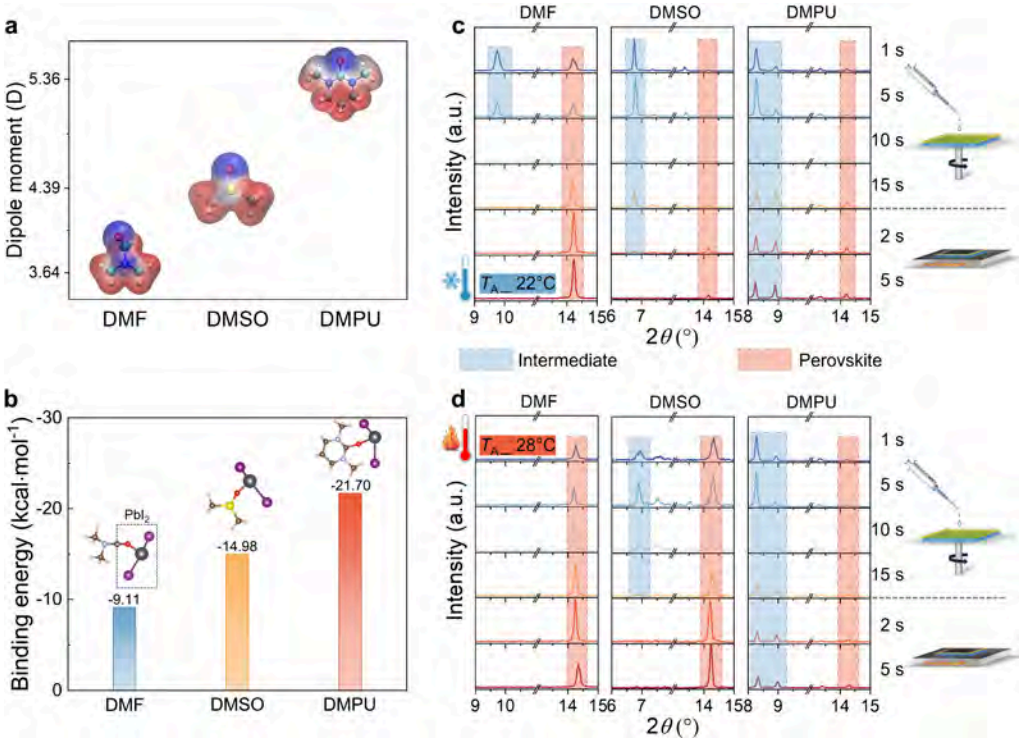

Figure 1. (a) Calculated partial charge distribution and dipole moment of DMF, DMSO, and DMPU. Blue and red represent more negative and positive charge density, respectively. (b) Binding energies of different solvent-coordinated adducts. The in situ XRD results of perovskite films (pure DMF, DMF/DMSO, and DMF/DMPU as the solvent) fabricated at a T_A of (c) 22 °C and (d) 28 °C. The "1 to 15 s" at the top refers to the continuous spin-coating time after dripping antisolvent. The "2 to 5 s" at the bottom refers to the annealing time.

that even small fluctuations of ambient conditions pose a threat on producing reliable PSCs. Recently, various approaches have been employed to improve the reproducibility of perovskite films. In 2021, Wang et al. introduced sulfolane as an additive in the perovskite precursor, which can form hydrogen bonding with methylammonium (MA) ions and then hinder the contact between precursor ions. This innovative method dramatically broadens the antisolvent treatment time window from 9 to 90 s.[21] In terms of the humidity window, Li et al. demonstrated that guanabenz acetate salt can eliminate both cation and anion vacancies, blocking the perovskite hydration and facilitating the crystallization of a high-quality film even in ambient air.[22] Furthermore, Xu et al. reported an ionic pair stabilizer, dimethylammonium formate, added into the perovskite precursor s to prevent the deprotonation of organic cations in humid air, thereby retarding the perovskite degradation. The researchers successfully fabricated high-efficiency PSCs (PCE of 24.72%) under ambient conditions with a relative humidity of 50%.[23] The aforementioned reports demonstrate the important role of additives in mitigating the ambient effect during the solution processing of perovskite film.

Although hitherto less explored, ambient temperature (T_A) also plays a significant role in determining the perovskite film quality. Saliba et al. demonstrated in 2018 that the PCE of PSCs was markedly reduced when the perovskite films were fabricated at a temperature above 27 °C inside a glovebox.[24] Similarly, Ye et al. also noted that the performance of FA-based PSCs fabricated in summer is inferior to that in winter due to crack formation on the film surface. To address this issue, the authors integrated a cooling system within the glovebox to lower the T_A to 18 °C, resulting in PSCs with largely enhanced performance.[25] Consequently, using temperature-controlled gloveboxes (≤20 °C) has become a standard practice, leading to the cessation of further investigation into the mechanisms of crack formation at elevated T_A. However, in terms of industry-scale applications, the cooling process increases the production cost and reduces the competitiveness in the PV market. Furthermore, limiting the fabrication process to a narrow T_A range significantly complicates the production control and negatively impacts the product yield in future scalable manufacturing. Therefore, it is critical to elucidate the intrinsic mechanism of the T_A effect on crack formation and to explore alternatives that can broaden the T_A processing window. Generally, a crack is referred to as a crystal fracture due to stress release during rapid crystal growth.[26,27] However, in our previous work, we noticed that the cracks in FA-based perovskite films form immediately right after the spin-coating, before the development of any large crystals.[28] Moreover, there is still a considerable amount of material present in the crack region, rather than void regions typically expected from stress release of the crystal plane. Such cracks are more likely a result of the inhomogeneous distribution of grains. Meanwhile, we also observed that the crack formation is always accompanied by a reduced amount of intermediate phase during the spin-coating. However, the intrinsic mechanism of crack formation and the influence of the intermediate phase on this process remain unclear. In addition, there is an urgent need to develop alternative strategies to replace conventional cooling methods to widen the processing windows for high-performance PSCs.

In this work, we report a solvent additive engineering strategy to control the nucleation kinetics in FA-based perovskites ($FA_{0.85}MA_{0.1}Cs_{0.05}PbI_3$), which involves adding 1,3-dimethyl-3,4,5,6-tetrahydro-2(1H)-pyrimidinone (DMPU) into the perovskite precursor for achieving PSCs with high

https://doi.org/10.1021/acsenergylett.4c03119
ACS Energy Lett. 2025, 10, 647−657

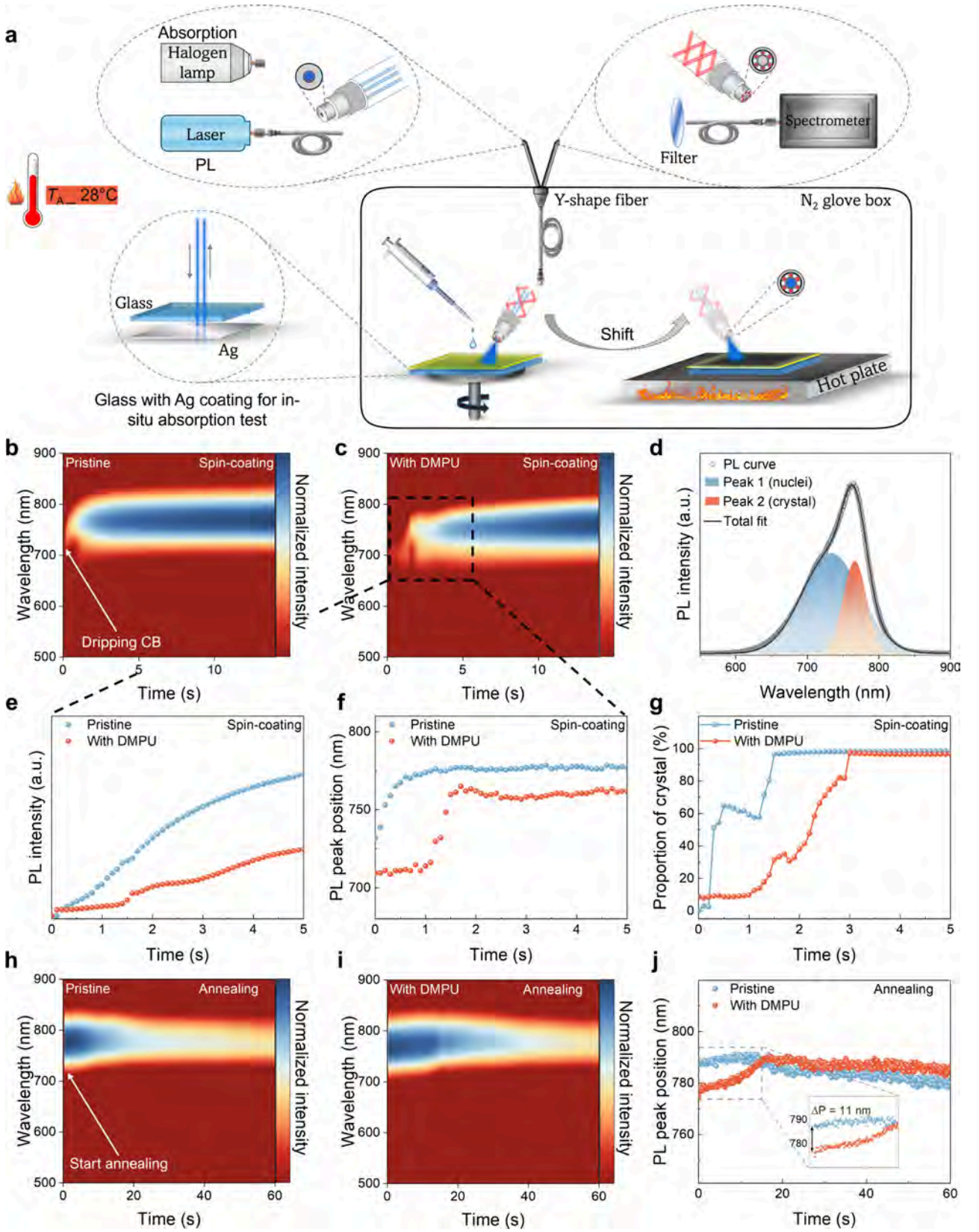

Figure 2. (a) Schematic diagram of the home-built in situ optical measure system. 2D contour plots of the in situ PL results obtained during the (b, c) spin-coating and (h, i) annealing processes. Extracted PL (e) intensity and (f) peak position evolution during the spin-coating process. (d) PL curve and Gauss fitting results. (g) Proportion of crystal phase evolution during the spin-coating process. (j) Extracted PL peak position evolution during the annealing process. All of the tests were conducted at a T_A of 28 °C.

https://doi.org/10.1021/acsenergylett.4c03119
ACS Energy Lett. 2025, 10, 647−657

performance even under a high T_A condition. The in situ X-ray diffraction (XRD) results reveal that the DMPU as a Lewis base can effectively coordinate with PbI_2 to form intermediate adducts across a T_A range of 22 to 28 °C. We further performed in situ optical experiments to monitor the crystallization dynamics of FA-based perovskite, which indicates that nucleation can be efficiently suppressed due to the strong bonding between the DMPU and PbI_2 in the perovskite precursor. Additionally, the formation of the DMPU-coordinated intermediate can compete with the crystallization process for precursor ions, which lowers the crystal growth rate. We found that the uniformly distributed DMPU adducts can prevent the nuclei from aggregation, thereby preventing solute depletion and suppressing crack formation. As a result, this approach greatly broadens the T_A processing window from 22 to 28 °C, achieving high-efficiency PSCs with PCE of 25.02% and 24.32%, respectively.

Our previous work reported that crack formation is strongly associated with the intermediate phase during the spin-coating process, which is determined by the selection of solvents.[28−30] In particular, for FA-based perovskite, the intermediate phase is a solvent adduct coordinated by the solvent molecules and PbI_2 in the precursor. In general, a Lewis base solvent with a high Gutmann donor number (DN) and boiling point (T_B) is easier to form solvent-adduct with PbI_2 due to its strong coordination ability and low volatility.[31] Compared to the conventional Lewis-bases, such as dimethylformamide (DMF) and DMSO (Supporting Information Figure S1), DMPU has a higher DN (~33 kcal·mol^{-1}) and T_B (~247 °C), thus exhibiting excellent potential to form a more stable solvent-coordinated intermediate to control the crystallization.

Figure 1a shows the calculated partial charge distribution of the various Lewis base solvent molecules, which present similar electron-rich oxygen moieties (blue) that can provide electrons to coordinate with Pb^{2+} ions to form Lewis adduct.[32] The slight shift of the S═O and C═O peaks in Fourier-transform infrared (FTIR) spectroscopy (Figure S2) further indicates that these Lewis base solvents possess the coordination capacity with PbI_2. Notably, the calculations also show that DMPU has the highest dipole moment of 5.36 D, in contrast to 3.64 D for DMF and 4.39 D for DMSO. This suggests a stronger tendency for DMPU to bond with PbI_2. Consequently, the binding energy (Figure 1b) of the DMPU-PbI_2 adduct (−21.70 kcal·mol^{-1}) is much higher than that of DMF and DMSO-coordinated adducts (−9.11 and −14.98 kcal·mol^{-1}, respectively), supporting that the DMPU can form more stable adducts. In fact, the adducts can also be observed even in the perovskite precursor (DMF/DMPU) probed by dynamic light scattering (DLS) measurement (Figure S3). The presence of such clusters can be further corroborated by the increase in absorption at ~375 nm in UV−vis spectra of the perovskite and PbI_2 precursors (Figure S4). We hypothesized that the strong bonding between DMPU and Pb^{2+} or I^- ions may suppress precursor ion coordination and, therefore, the nucleation during the spin-coating process.

We sought to investigate the impact of DMPU on the phase evolution of FA-based perovskite ($FA_{0.85}MA_{0.1}Cs_{0.05}PbI_3$) during spin-coating and subsequent annealing under different T_A conditions (22 and 28 °C) by in situ XRD measurements. It is worth noting that only the beginning of the annealing process (0 to 5 s) is considered, as the phase transformation of the intermediate phase and the perovskite phase mainly occur within the time window. In the case of a low T_A condition (22 °C), as shown in Figure 1c, the peaks corresponding to the intermediate phase (blue box region) are detected in all three types of wet perovskite films right after dripping the antisolvent chlorobenzene (CB).[2,17,33] Unlike the films using DMF and DMF/DMSO as solvents, the intermediate phase in the DMPU-treated film persists throughout the subsequent spin-coating and thermal annealing processes, indicating that the DMPU-coordinated intermediate phase is more stable. Moreover, thermogravimetric analysis (TGA), as shown in Figure S5, also reveals slower evaporation in DMPU-treated perovskite ink, further explaining the prolonged existence of the DMPU-coordinated intermediate phase. On the other hand, the α-phase (red box region) of the perovskite peak in the film prepared with DMPU is significantly weaker than the intermediate phase peak, suggesting the DMPU indeed suppresses the crystallization of the α-phase perovskite. Interestingly, once the T_A increases to 28 °C, as shown in Figure 1d, no intermediate phase peak is detected in the perovskite film prepared with DMF, which may be attributed to the weaker coordination capacity of DMF with PbI_2 and the DMF molecules are readily evaporated even at this slightly escalated temperature. Although the intermediate phase still exists in the DMSO-treated perovskite film, the corresponding diffraction intensity decreases significantly with increasing T_A. Meanwhile, the intensity of the α-phase perovskite peak in the DMSO-treated film increases greatly at the higher T_A condition of 28 °C, suggesting an accelerated crystallization process. In contrast, there is no noticeable change in the intermediate phase peaks of the DMPU-treated perovskite film, even when the T_A is elevated from 22 to 28 °C. This indicates that the proposed Lewis base solvent, DMPU, interacts more effectively with PbI_2 to form a stable solvent adduct than conventional solvents (DMF and DMSO).

Based on the in situ XRD results, the stability of the intermediate phase in different solvent-treated perovskites varies significantly when the T_A is increased to 28 °C. Hence, we sought to further investigate the impact of the DMPU-coordinated adducts on the perovskite nucleation and crystallization processes under a T_A of 28 °C in detail via in situ optical techniques. Figure 2a shows the home-built in situ optical setup for photoluminescence (PL) and absorption measurements, the setup is housed inside the same temperature-regulated nitrogen-filled glovebox used for the spin-coating and annealing processes.[28,34,35] Panels b and c of Figure 2 show the 2D contour plots of the in situ PL results obtained during the spin-coating under a high T_A condition (28 °C). The sample prepared with DMF/DMSO (4:1 (vol %)) as the solvent is labeled as "Pristine", whereas the sample with DMF/DMSO/DMPU (8:1.5:0.5 (vol %)) as the solvent is labeled as "With DMPU". The "0 s" in the x-axis represents the time for dripping the antisolvent (CB), where the nucleation is started, and a noticeable PL signal can be recorded. Both pristine and DMPU-treated samples reach a readily PL intensity and wavelength (775 and 755 nm, respectively) after 10 s of spin-coating time. However, their PL signals are significantly different in the first few seconds after dripping the CB, which is further analyzed and replotted as shown in Figure 2e,f. In the case of the pristine sample, there is a rapid increase in the PL intensity, two times higher than that in the DMPU-treated sample. Meanwhile, the PL peak position in the pristine sample redshifts steeply from 725 to 775 nm within the first 1 s. In contrast, the wavelength is kept constant at 710 nm in the DMPU-treated sample during the first 1 s. On

https://doi.org/10.1021/acsenergylett.4c03119
ACS Energy Lett. 2025, 10, 647−657

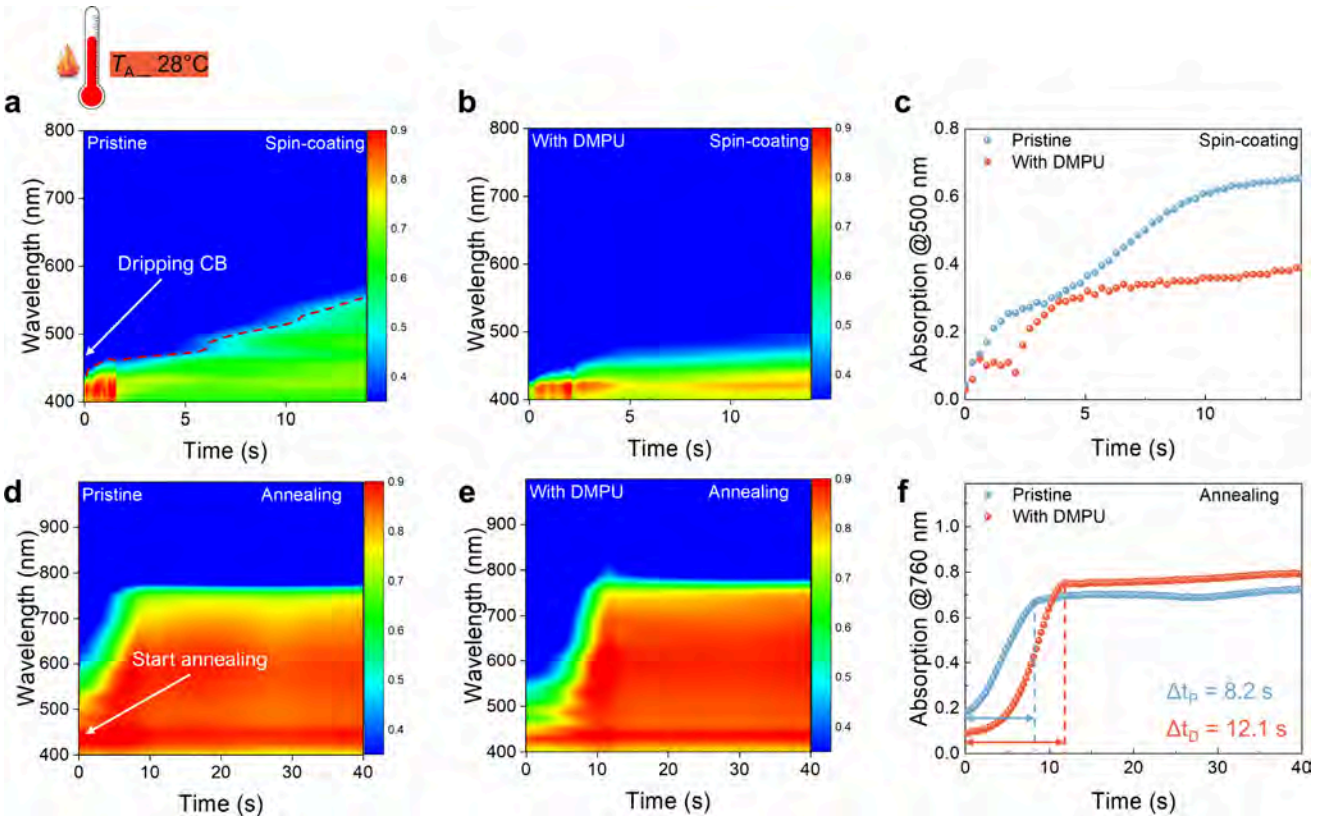

Figure 3. 2D contour plots of the in situ UV−vis absorption data obtained during the (a, b) spin-coating and (d, e) annealing processes. The extracted absorption intensity evolution at (c) 500 nm during spin-coating and (f) 760 nm during annealing. All of the tests were conducted at a T_A of 28 °C.

the one hand, the slower increase in the PL intensity in the DMPU-treated sample indicates a small number of luminous nuclei formed, which is a sign of retarded nucleation. This may be attributed to the strong bonding between DMPU and Pb^{2+} ions mentioned before. On the other hand, the initial constant wavelength in the first 1 s in the DMPU-treated sample suggests a retarded growth of the formed nuclei, and the PL at 710 nm indicated a certain degree of quantum confinement.[36−38] This behavior reflects the fact the intermediate phase has already been formed in the precursor, which is supported by the DLS observation of large aggregates in the precursor. The later increase in the PL wavelength and intensity in the DMPU-treated sample is possibly due to the increased precursor concentration with the evaporation of the solvent and the concurrent growth of perovskite nuclei during the later stage of spin coating.

It is noteworthy that the PL spectral line shape obtained during the spin-coating is generally asymmetrical. The films at this early stage of crystallization consist of a mixture of perovskite nuclei and bulk crystal phases with different emission wavelengths. The PL curves can be fitted with two Gaussian peaks as shown in Figure 2d (the fitting results are presented in Figure S6). The peak centered at 770 nm corresponds to the perovskite crystal phase with a size larger than 10 nm and negligible quantum confinement effect,[39,40] whereas the other peak with a position that varies with time corresponds to the growing nuclei. Consequently, as shown in Figure 2g, we can reveal the evolution of the ratio between the perovskite nuclei and crystal by comparing the integrated intensities of the two fitted Gaussian peaks. This approach allows a more accurate evaluation of the time required for reaching the stage of complete nucleation. In the case of the pristine sample, there is a steep increase in the proportion of the perovskite crystal phase from 0% to 99% within around 1.5 s. In contrast, the crystal proportion in the DMPU-treated sample is kept constant at 10% during the initial 1 s then, followed by a steady increase, reaching 99% at around 3 s. Indicating that the DMPU can effectively retard the growth from perovskite nuclei to crystal phases even at a high T_A condition. Moreover, the in situ PL results obtained during annealing further support this conclusion. As shown in Figure 2h−j, after transferring the samples to the hot plate, a distinct red shift (~11 nm) in the PL peak position is detected within 15 s in the DMPU-treated sample, suggesting an incomplete conversion from perovskite nuclei to bulk phases during the previous spin-coating process. It is believed that the incomplete conversion can be attributed to retarded crystallization caused by the stable DMPU-coordinated intermediate phase, details of the mechanism will be discussed below.

To further understand the crystallization dynamics, we performed in situ optical absorption measurements of the samples during spin-coating and annealing. The absorption results can provide insights on the evolution of any material that is not light-emitting. In terms of the pristine sample during spin-coating (Figure 3a), the absorption edge continuously redshifts toward a longer wavelength (around 600 nm). In contrast, as shown in Figure 3b, the absorption edge of the DMPU-treated film maintains the characteristic absorption of intermediate phases (400−450 nm). Since the intermediate phase only absorbs up to 450 nm, the growth of perovskite can be monitored with the absorption changes in the longer

https://doi.org/10.1021/acsenergylett.4c03119
ACS Energy Lett. 2025, 10, 647−657

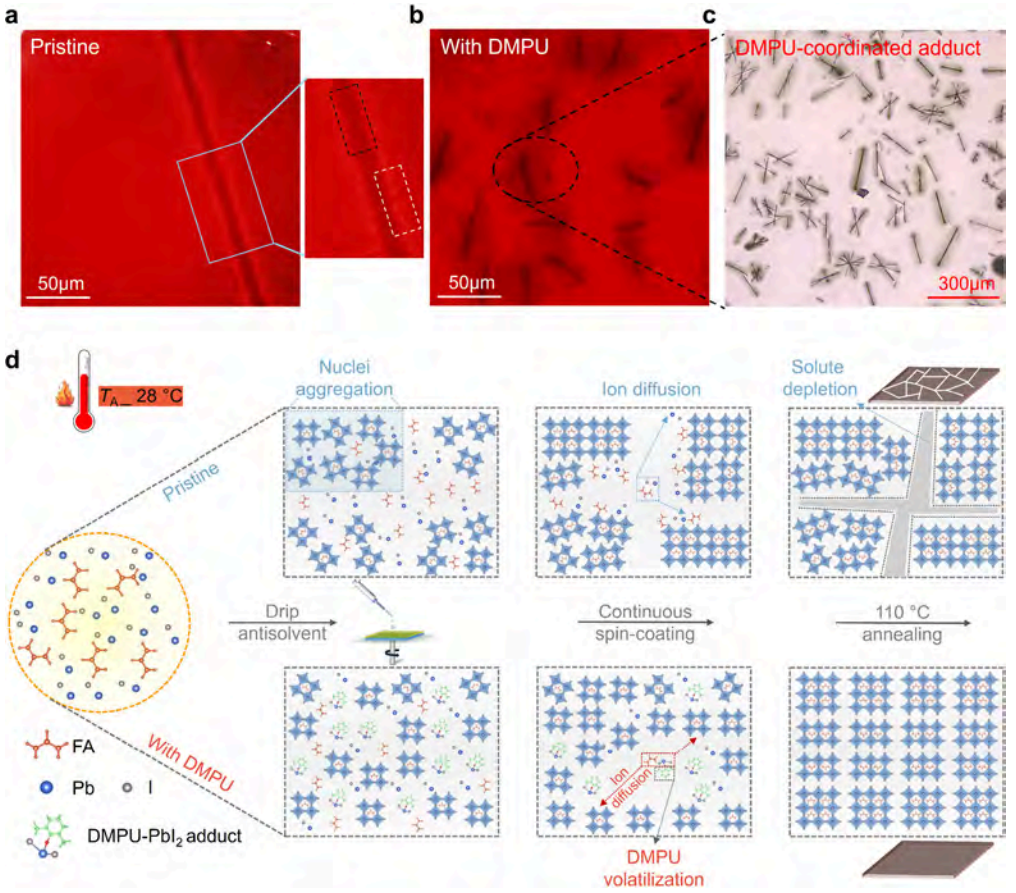

Figure 4. Confocal microscopy images of the as-cast (a) pristine and (b) DMPU-treated perovskite film fabricated at a T_A of 28 °C. (c) Optical microscopy images of the wet FAI-PbI_2-DMPU film without antisolvent treatment. (d) Schematic diagram of possible phase evolution in the nucleation and crystallization of pristine and DMPU-treated FA-based perovskites under a T_A of 28 °C.

wavelength regine.[19,41] As shown in Figure 3c, the absorption of the pristine sample at 500 nm immediately increased upon dripping the antisolvent and reached the first plateau in 3 s, then continued to increase until reaching the second plateau in 10 s. Interestingly, in the case of the DMPU-treated sample, there is an initial delay of absorption increase, as similarly observed in the in situ PL results. Then, the absorption only increased for 3 s to reach the plateau region. Considering the complementary in situ PL results, we conclude that the first increase in absorption corresponds to the nucleation, and the second increase that is only observed in the pristine sample corresponds to the additional nuclei growth and crystallization due to nuclei aggregation. According to the in situ PL and absorption results, the nucleation and crystallization are more efficient in the pristine sample at such a high T_A. However, adding DMPU can suppress the aggregation, the DMPU-treated sample only shows a slight increase in absorption at the beginning of the spin-coating. The in situ absorption results during the subsequent thermal annealing further support the different nucleation dynamics between the samples. The full transition to the perovskite bulk phase in the DMPU-treated sample is completed at 12.1 s, as opposed to 8.2 s for the pristine sample (Figure 3d–f), indicative of the retention of DMPU-coordinated intermediate phase and retarded intermolecular exchange process in the DMPU-treated sample.

More importantly, the DMPU-treated film presents similar PL and absorption evolution processes at low and high T_A from 22 to 28 °C, as shown in Figures S7–S11, in stark contrast to the pristine film. Indicating that DMPU can result in controllable and orderly nucleation and crystallization, decreasing the sensitivity of perovskite to the T_A, which is important for improving the reproducibility of perovskite film fabricated under different T_A conditions.

Panels a and b of Figure 4 show the confocal microscopy images of as-cast pristine and DMPU-treated perovskite films fabricated at a T_A of 28 °C, aiming to gain a deeper understanding of the mechanism of suppressed nuclei aggregation with DMPU-assisted intermediate phase. In the case of the pristine film, there is a dark line-shaped region (black dotted box) flanked by relatively bright regions (white dotted box). In contrast, the DMPU-treated film shows no such dark lines, but numerous needle-shaped nonluminous phases are distributed across the surface. The dark line in the pristine film turned out to be a crack on the film surface, composed of less luminous perovskite crystals compared to the surrounding areas. The majority of bright regions on both sides indicate the formation of adequate luminous phases, supporting the observed nuclei aggregation in the in situ absorption results. On the other hand, the needle-shaped phase in the DMPU-treated sample is the intermediate phase, as verified by the optical microscopy image of the wet perovskite film using pure DMPU as the solvent without antisolvent dripping (Figure 4c). These results suggest that the distribution of intermediate phase is crucial for suppressing crack formation.

https://doi.org/10.1021/acsenergylett.4c03119
ACS Energy Lett. 2025, 10, 647–657

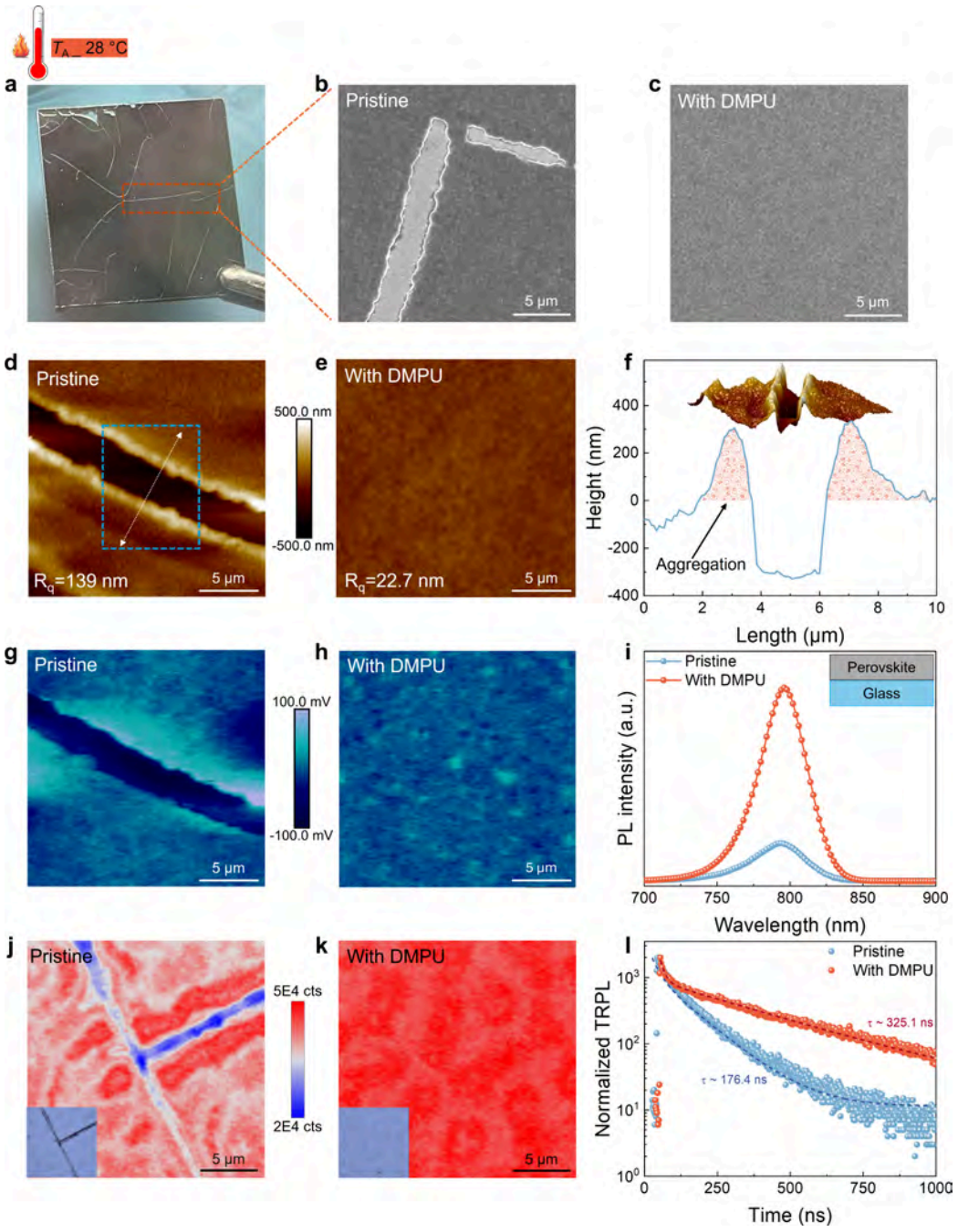

Figure 5. (a) Photograph of annealed perovskite film with cracks. (b, c) SEM, (d, e) AFM, (g, h) KPFM, and (j, k) PL intensity mapping images, (i) steady state PL, and (l) TRPL curves of annealed pristine and DMPU-treated perovskite films. (f) Topography line scans indicated by arrows in panel d.

Based on the in situ optical measurements results and confocal microscopy images, the crystal formation dynamics during the FA-based perovskite fabrication process under a high T_A condition are illustrated in Figure 4d. For the solution-processed fabrication of perovskite thin films, nucleation and crystallization are critical in determining the film quality. During nucleation, the solute concentration increases to a supersaturation level, triggering the precipitation and formation of nuclei. During crystallization, ions and nuclei undergo thermally driven mutual diffusion, leading to the growth of nuclei into larger crystals. These two processes often occur simultaneously. For the pristine sample, the fast evaporation of uncoordinated solvent molecules during spin-coating facilitates rapid nucleation and crystallization. In particular, the thermally driven nuclei collisions at a high T_A leads to strong nuclei aggregation. Resulting in solute depletion and crack formation in the perovskite film. In contrast, the addition of DMPU mediates the formation of robust intermediate adducts by coordinating with PbI_2 during spin-coating, which can consume the precursor ions, effectively retarding the initial nucleation and crystal growth. Meanwhile, the homogeneously distributed intermediates can act as a physical barrier to efficiently reduce the thermally driven nuclei collision, preventing nuclei aggregation. In addition, due to the high boiling point, DMPU volatilizes slowly during the subsequent spin-coating and annealing process, allowing Pb^{2+}

https://doi.org/10.1021/acsenergylett.4c03119
ACS Energy Lett. 2025, 10, 647−657

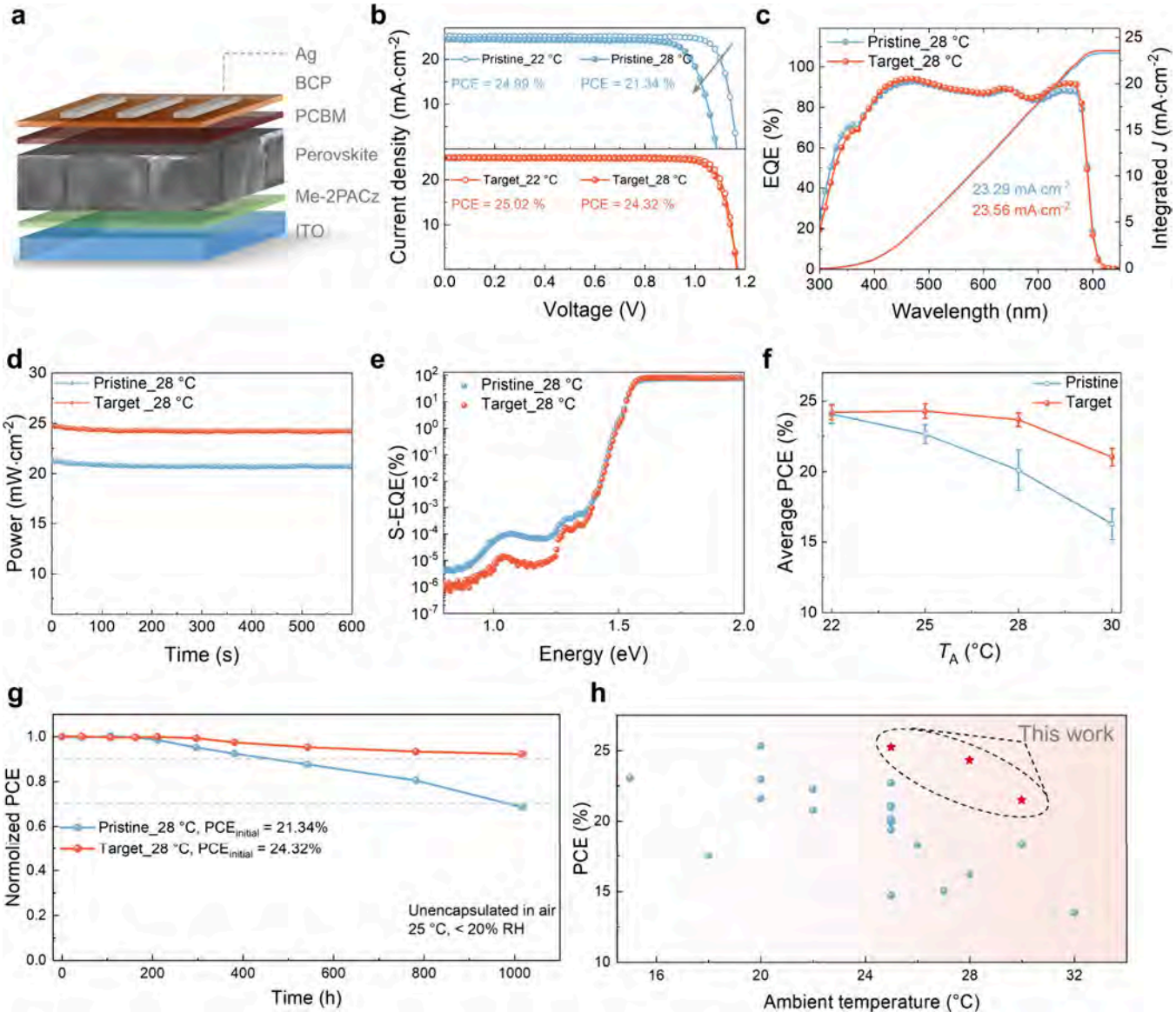

Figure 6. (a) Schematic diagram of PSCs structure in this work. (b) $J-V$ curves of pristine and target PSCs fabricated under different T_A conditions. (c) EQE spectra, (d) SPO results, and (e) S-EQE spectra of pristine and target samples fabricated at a T_A of 28 °C. (f) Average PCE of PSCs fabricated under different T_A conditions. (g) Shelf lifetime of unencapsulated devices. (h) Comparison with reported PCE of PSCs fabricated under different T_A conditions.

and I- ions to be steadily released from DMPU-coordinated intermediate adducts and thereby achieving orderly and controllable crystallization, leading to the synthesis of high-quality films.

We further examined the impacts of the DMPU on the properties of the perovskite films fabricated under different T_A conditions, focusing on morphology, crystallinity, and optoelectronic characteristics. Panels a and b of Figure 5 show the top-view scanning electron microscopy (SEM) images of the pristine perovskite film synthesized at a T_A of 28 °C. A large number of cracks were observed on the surface with a width of 3 μm. In contrast, the DMPU-treated film exhibits a smooth and flat surface (Figure 5c). In the crack-free regions, a similar grain size distribution (500−800 nm) is observed in both perovskite films (Figure S12). Moreover, atomic force microscopy (AFM) was performed to analyze the grain distribution adjacent to the crack region, as shown in Figures 5d,e. Due to the existence of the crack, the root-mean-square roughness (Rq) of the pristine film is much higher than that of the DMPU-treated film (139.0 and 22.7 nm, respectively). Furthermore, Figure 5f gives the height variation in the cross-line profile and the corresponding 3D image (blue dotted box region in Figure 5d). It is worth noting that the depth of the crack region is around 600 nm, with significant material aggregation detected on both sides of the crack, indicating that the crack formation results from the inhomogeneous growth and distribution of grains induced by solute depletion, rather than the commonly held belief of stress release.

Moreover, Kelvin probe force microscopy (KPFM) was used to investigate the potential distribution of the perovskite film surfaces. Compared to the pristine film, the DMPU-treated film exhibits a uniform potential distribution, which can be attributed to the more homogeneous surface morphology (Figure 5g,h). Furthermore, as shown in Figure 5i, the DMPU-treated film shows a 4-fold enhancement in PL intensity,

https://doi.org/10.1021/acsenergylett.4c03119
ACS Energy Lett. 2025, 10, 647−657

indicative of reduced nonradiative recombination. Meanwhile, time-resolved PL (TRPL) decay reveals a prolonged PL lifetime of 325.1 ns in the DMPU-treated film, nearly twice as long as that of the pristine film (176.4 ns), as shown in Figure 5l. Demonstrating that the DMPU-treated film has higher quality with fewer defect-induced nonradiative recombination sites. Additionally, PL intensity mapping images (Figure 5j,k) show a more uniform and higher fluorescence intensity in the DMPU-treated perovskite film, indicating a homogeneous grain distribution and less nonradiative recombination, consistent with steady-state PL results. Interestingly, the PL peak position mapping image (Figure S13) shows that the crack region has longer wavelength emission, which indicates the segregation of FA-rich phases with a smaller band gap, further supporting the nuclei aggregation.

In addition, the morphology investigation of films, with or without DMPU treatment, was further conducted under different T_A conditions, as shown in Figures S14−S19. The morphology of the pristine film significantly deteriorates as the T_A increases, in stark contrast to the DMPU-optimized film. Besides morphology, the crystallinity of pristine film also decreases with the temperature increase, albeit with the optical absorption remaining unaffected (Figures S20 and S21). The differences in perovskite film quality at different T_A reveal that DMPU additive effectively reduces the temperature sensitivity of the one-step fabrication process, broadening the T_A processing window for fabricating high-quality perovskite films.

In this work, we fabricated PSCs with the p-i-n configuration of indium tin oxide (ITO)/Me-2PACz//PCBM/BCP/Ag (Figure 6a) under different T_A conditions. First, the volume ratio of DMPU in the precursor was tuned to optimize perovskite film quality and PV device performance. It is found that the film prepared from a precursor with a higher concentration of DMPU additive (10%) exhibits a significantly high surface roughness (R_q = 110 nm) despite the absence of crack formation, as shown in Figure S22. The rough surface may be attributed to the disorderly Ostwald ripening, as a consequence of excessively slow solvent evaporation. This high surface roughness negatively impacts the device's performance, as shown in Figure S23. As a result of optimization, the PSCs fabricated with a mixed solvent of DMF: DMSO: DMPU = 8:1.3:0.7 (vol %) showed the optimal performance, which is denoted as the Target.

At a T_A of 22 °C, the pristine and target devices possess similar performance with a PCE of 24.99% and 25.02%, respectively. However, when fabricated at a T_A of 28 °C, the PCE of the champion target device improved from 21.34% to 24.32% after adding DMPU, with an open-circuit voltage (V_{OC}) increasing from 1.09 to 1.17 V and the fill factor (FF) from 80.26% to 83.65%, under the reverse current−voltage sweep (Figure 6b and Table S1, corresponding forward data are given in Figure S24 and Table S2). Figures 6c and S25 present the integrated current density calculated from the external quantum efficiency (EQE) measurement matched closely with the short current density (J_{SC}) obtained from the J−V curves. Meanwhile, the stabilized power output (SPO) of the target PSC at the maximum power point (MPP) under 1 sun illumination is 24.19 mW·cm^{-2} (Figure 6d), which aligns with the PCE from the J−V curve. The device performance statistics are shown in Figure S26.

Furthermore, we investigated the defects in the pristine and target devices by measuring their sub-bandgap EQE (S-EQE) spectra. As shown in Figures 6e and S27, the Urbach tails of the two devices are very similar. However, the S-EQE signal in the target device is much lower in the entire sub-bandgap region from 1.5 to 0.8 eV, suggesting a smaller number of defects in the target film. We further analyzed the difference in defects between the two devices by subtracting the S-EQE spectrum of the pristine from the spectrum of the target device. As shown in Figure S28, several distinctive peaks can be found at 1.1 and 1.4 eV. According to the previously calculated defect transition energy levels in similar systems of $FAPbI_3$ and $MAPbI_3$, the 1.1 eV transition corresponds to the interstitial and antisite defects of Pb_I, and the 1.4 eV transition corresponds to the FA_I interstitial.[35,42] Hence, the analysis of the S-EQE results hints that the defects in $FAMAPbI_3$ are mainly associated with the FA and the halide components, which is consistent with the aforementioned FA-rich phase segregation around the crack region. In addition, the target films exhibited less nonradiative recombination losses, lower leakage current density, smaller deviation factor (1.47), and lower trap density (1.76×10^{-15} cm^{-3}), as determined by electrochemical impedance spectroscopy (EIS), dark J−V plots, V_{OC}-light-dependent plots, and space-charge-limited current (SCLC) measurements (Figure S29)

In general, the reproducible performance of PSCs fabricated within a processing temperature window as wide as possible is crucial for the commercialization of the technology. The conventional one-step processed FA-based perovskite film quality is highly sensitive to the T_A level (Figure 6f): The average PCE decreased from 24.5% to 16.2% as the T_A increased from 22 to 30 °C, accompanied by broader performance distributions. We find that adding DMPU in the precursor can significantly improve the reproducibility of PSCs across a wide range of T_A: The target devices achieved PCEs of >24% across T_A from 22 to 28 °C and reached a PCE of 21.8% even at a T_A of 30 °C, which we ascribed to the orderly and homogeneous crystallization induced by the more stable DMPU-coordinated intermediate phases. In addition, we further performed MPP tracking of encapsulated PSCs (Figure S30), the target PSC maintains over 90% of its initial PCE after more than 200 h of continuous operation in the air (25 °C, 50−60% RH). Moreover, the shelf lifetime of the unencapsulated PSCs was in the air (25 °C, < 20% RH), as shown in Figure 6g. The target device maintains 90% of the initial PCE of 24.32% after 1000 h storage, compared with 70% of the initial PCE of 21.34% for the pristine device. The efficiencies for PSCs fabricated under different T_A conditions reported in the literature are summarized in Figure 6h, with detailed PV parameters summarized in Tables S3.

In summary, this work revealed that the narrow T_A processing window in FA-based perovskites originated from the thermally activated nuclei aggregation during solution processing. Lowing the processing temperature below 22 °C is often required to ensure perovskite film quality and reproducibility, which, however, reduces the competitiveness of the technology in low-cost and large-scale production. We found that the DMPU solvent additive could form a stable intermediate phase that is resistant to dissociation in a wide temperature range. During the spin-coating and annealing steps, the intermediate phase is essential to ensure a homogeneous nucleation process by not only controlling the release of precursor ions but, more importantly, preventing the nuclei from excessive aggregation. By regulating the grain growth with an optimized DMPU ratio in the solvent, we consistently achieved PCEs of over 24% in PSCs fabricated in a

https://doi.org/10.1021/acsenergylett.4c03119
ACS Energy Lett. 2025, 10, 647−657

wide range of T_A from 22 to 28 °C, paving the way for realizing the long-sought reliable large-scale production.

■ ASSOCIATED CONTENT

Supporting Information

The Supporting Information is available free of charge at https://pubs.acs.org/doi/10.1021/acsenergylett.4c03119.

Details regarding experimental methods; FTIR; DLS; UV−vis absorption; TGA; in situ PL and absorption; SEM; AFM; KPFM; PL peak position mapping; PL; TRPL; XRD; $J-V$ curves; EQE; S-EQE; SCLC; EIS; MPP tracking results and statistics of photovoltaic parameters of pristine and target devices (PDF)

■ AUTHOR INFORMATION

Corresponding Authors

Sai Wing Tsang − *Department of Materials Science and Engineering and Center of Super-Diamond and Advanced Films (COSDAF) and Hong Kong Institute for Clean Energy, City University of Hong Kong, Hong Kong SAR 999077, People's Republic of China;* orcid.org/0000-0003-0788-4905; Email: saitsang@cityu.edu.hk

Tom Wu − *Department of Applied Physics, The Hong Kong Polytechnic University, Hong Kong SAR 999077, People's Republic of China;* orcid.org/0000-0003-0845-4827; Email: tom-tao.wu@polyu.edu.hk

Authors

Yunfan Wang − *Department of Materials Science and Engineering, City University of Hong Kong, Hong Kong SAR 999077, People's Republic of China*

Zhuoqiong Zhang − *Department of Applied Physics, The Hong Kong Polytechnic University, Hong Kong SAR 999077, People's Republic of China*

Zixin Zeng − *Department of Materials Science and Engineering, City University of Hong Kong, Hong Kong SAR 999077, People's Republic of China*

Yuxuan Zhang − *Department of Materials Science and Engineering, City University of Hong Kong, Hong Kong SAR 999077, People's Republic of China*

Tianli Hu − *Department of Biomedical Engineering, City University of Hong Kong, Hong Kong SAR 999077, People's Republic of China*

Leyu Bi − *Department of Chemistry, City University of Hong Kong, Hong Kong SAR 999077, People's Republic of China*

Yajie Yang − *Institute of New Energy and Low-Carbon Technology & College of Materials Science and Engineering, Sichuan University, Chengdu 610064, People's Republic of China*

Shanchao Ouyang − *Department of Materials Science and Engineering, City University of Hong Kong, Hong Kong SAR 999077, People's Republic of China*

Xia Hao − *Institute of New Energy and Low-Carbon Technology & College of Materials Science and Engineering, Sichuan University, Chengdu 610064, People's Republic of China;* orcid.org/0000-0002-3512-9600

Chenjie Xu − *Department of Biomedical Engineering, City University of Hong Kong, Hong Kong SAR 999077, People's Republic of China;* orcid.org/0000-0002-8278-3912

Yuanhang Cheng − *School of New Energy, Nanjing University of Science and Technology, Jiangyin, Jiangsu 21443, People's Republic of China*

Hanlin Hu − *Hoffmann Institute of Advanced Materials, Shenzhen Polytechnic University, Shenzhen 518055, People's Republic of China;* orcid.org/0000-0001-5617-0998

Alex K.-Y. Jen − *Department of Materials Science and Engineering, Department of Chemistry, and Center of Super-Diamond and Advanced Films (COSDAF) and Hong Kong Institute for Clean Energy, City University of Hong Kong, Hong Kong SAR 999077, People's Republic of China;* orcid.org/0000-0002-9219-7749

Johnny C. Ho − *Department of Materials Science and Engineering, City University of Hong Kong, Hong Kong SAR 999077, People's Republic of China;* orcid.org/0000-0003-3000-8794

Complete contact information is available at: https://pubs.acs.org/10.1021/acsenergylett.4c03119

Author Contributions

◆Y.W. and Z. Zhang contributed equally to this work.

Notes

The authors declare no competing financial interest.

■ ACKNOWLEDGMENTS

We acknowledge the General Research Fund (CityU 11304420 and 11317422) from the Research Grants Council of Hong Kong SAR, China.

■ REFERENCES

(1) Kojima, A.; Teshima, K.; Shirai, Y.; Miyasaka, T. Organometal halide perovskites as visible-light sensitizers for photovoltaic cells. *J. Am. Chem. Soc.* **2009**, *131* (17), 6050−6051.

(2) Jeon, N. J.; Noh, J. H.; Kim, Y. C.; Yang, W. S.; Ryu, S.; Seok, S. I. Solvent engineering for high-performance inorganic−organic hybrid perovskite solar cells. *Nat. Mater.* **2014**, *13* (9), 897−903.

(3) Wang, Y.; Xiang, P.; Ren, A.; Lai, H.; Zhang, Z.; Xuan, Z.; Wan, Z.; Zhang, J.; Hao, X.; Wu, L.; et al. MXene-modulated electrode/SnO2 interface boosting charge transport in perovskite solar cells. *ACS Appl. Mater. Interfaces* **2020**, *12* (48), 53973−53983.

(4) Green, M. A.; Dunlop, E. D.; Yoshita, M.; Kopidakis, N.; Bothe, K.; Siefer, G.; Hinken, D.; Rauer, M.; Hohl-Ebinger, J.; Hao, X. Solar cell efficiency tables (Version 64). *Progress in Photovoltaics* **2024**, *32* (7), 425−441.

(5) Green, M. A.; Dunlop, E. D.; Yoshita, M.; Kopidakis, N.; Bothe, K.; Siefer, G.; Hinken, D.; Rauer, M.; Hohl-Ebinger, J.; Hao, X. Solar cell efficiency tables (Version 64). *Prog. Photovolt* **2024**, *32* (7), 425−441.

(6) Yang, T.; Gao, L.; Lu, J.; Ma, C.; Du, Y.; Wang, P.; Ding, Z.; Wang, S.; Xu, P.; Liu, D.; et al. One-stone-for-two-birds strategy to attain beyond 25% perovskite solar cells. *Nat. Commun.* **2023**, *14* (1), 839.

(7) Saki, Z.; Byranvand, M. M.; Taghavinia, N.; Kedia, M.; Saliba, M. Solution-processed perovskite thin-films: the journey from lab-to large-scale solar cells. *Energy Environ. Sci.* **2021**, *14* (11), 5690−5722.

(8) Liu, C.; Cheng, Y.-B.; Ge, Z. Understanding of perovskite crystal growth and film formation in scalable deposition processes. *Chem. Soc. Rev.* **2020**, *49* (6), 1653−1687.

(9) He, R.; Wang, W.; Yi, Z.; Lang, F.; Chen, C.; Luo, J.; Zhu, J.; Thiesbrummel, J.; Shah, S.; Wei, K.; et al. Improving interface quality for 1-cm2 all-perovskite tandem solar cells. *Nature* **2023**, *618* (7963), 80−86.

(10) Lin, R.; Xiao, K.; Qin, Z.; Han, Q.; Zhang, C.; Wei, M.; Saidaminov, M. I.; Gao, Y.; Xu, J.; Xiao, M.; et al. Monolithic all-perovskite tandem solar cells with 24.8% efficiency exploiting comproportionation to suppress Sn (ii) oxidation in precursor ink. *Nat. Energy* **2019**, *4* (10), 864−873.

(11) Lee, J.-W.; Tan, S.; Seok, S. I.; Yang, Y.; Park, N.-G. Rethinking the A cation in halide perovskites. *Science* **2022**, *375* (6583), No. eabj1186.
(12) Prakash, J.; Singh, A.; Sathiyan, G.; Ranjan, R.; Singh, A.; Garg, A.; Gupta, R. K. Progress in tailoring perovskite based solar cells through compositional engineering: Materials properties, photovoltaic performance and critical issues. *Mater. Today Energy* **2018**, *9*, 440−486.
(13) Jung, H. S.; Park, N. G. Perovskite solar cells: from materials to devices. *small* **2015**, *11* (1), 10−25.
(14) Li, Z.; Klein, T. R.; Kim, D. H.; Yang, M.; Berry, J. J.; Van Hest, M. F.; Zhu, K. Scalable fabrication of perovskite solar cells. *Nat. Rev. Mater.* **2018**, *3* (4), 18017.
(15) Yang, M.; Li, Z.; Reese, M. O.; Reid, O. G.; Kim, D. H.; Siol, S.; Klein, T. R.; Yan, Y.; Berry, J. J.; van Hest, M. F. A. M.; Zhu, K. Perovskite ink with wide processing window for scalable high-efficiency solar cells. *Nature Energy* **2017**, *2* (5), 17038.
(16) Chen, H.; Liu, C.; Xu, J.; Maxwell, A.; Zhou, W.; Yang, Y.; Zhou, Q.; Bati, A. S.; Wan, H.; Wang, Z.; et al. Improved charge extraction in inverted perovskite solar cells with dual-site-binding ligands. *Science* **2024**, *384* (6692), 189−193.
(17) Wang, R.; Zhu, J.; You, J.; Huang, H.; Yang, Y.; Chen, R.; Wang, J.; Xu, Y.; Gao, Z.; Chen, J.; et al. Custom-tailored solvent engineering for efficient wide-bandgap perovskite solar cells with a wide processing window and low V OC losses. *Energy Environ. Sci.* **2024**, *17* (7), 2662−2669.
(18) Cheng, Y.; Xu, X.; Xie, Y.; Li, H. W.; Qing, J.; Ma, C.; Lee, C. S.; So, F.; Tsang, S. W. 18% high-efficiency air-processed perovskite solar cells made in a humid atmosphere of 70% RH. *Solar RRL* **2017**, *1* (9), 1700097.
(19) Zou, Y.; Yu, W.; Guo, H.; Li, Q.; Li, X.; Li, L.; Liu, Y.; Wang, H.; Tang, Z.; Yang, S.; et al. A crystal capping layer for formation of black-phase FAPbI3 perovskite in humid air. *Science* **2024**, *385* (6705), 161−167.
(20) Li, N.; Niu, X.; Li, L.; Wang, H.; Huang, Z.; Zhang, Y.; Chen, Y.; Zhang, X.; Zhu, C.; Zai, H.; et al. Liquid medium annealing for fabricating durable perovskite solar cells with improved reproducibility. *Science* **2021**, *373* (6554), 561−567.
(21) Huang, H.-H.; Liu, Q.-H.; Tsai, H.; Shrestha, S.; Su, L.-Y.; Chen, P.-T.; Chen, Y.-T.; Yang, T.-A.; Lu, H.; Chuang, C.-H.; et al. A simple one-step method with wide processing window for high-quality perovskite mini-module fabrication. *Joule* **2021**, *5* (4), 958−974.
(22) Yan, L.; Huang, H.; Cui, P.; Du, S.; Lan, Z.; Yang, Y.; Qu, S.; Wang, X.; Zhang, Q.; Liu, B.; et al. Fabrication of perovskite solar cells in ambient air by blocking perovskite hydration with guanabenz acetate salt. *Nat. Energy* **2023**, *8* (10), 1158−1167.
(23) Meng, H.; Mao, K.; Cai, F.; Zhang, K.; Yuan, S.; Li, T.; Cao, F.; Su, Z.; Zhu, Z.; Feng, X.; et al. Inhibition of halide oxidation and deprotonation of organic cations with dimethylammonium formate for air-processed p−i−n perovskite solar cells. *Nat. Energy* **2024**, *9*, 536−547.
(24) Saliba, M.; Correa-Baena, J.-P.; Wolff, C. M.; Stolterfoht, M.; Phung, N.; Albrecht, S.; Neher, D.; Abate, A. How to Make over 20% Efficient Perovskite Solar Cells in Regular (n−i−p) and Inverted (p−i−n) Architectures. *Chem. Mater.* **2018**, *30* (13), 4193−4201.
(25) Ye, J.; Liu, G.; Jiang, L.; Zheng, H.; Zhu, L.; Zhang, X.; Wang, H.; Pan, X.; Dai, S. Crack-free perovskite layers for high performance and reproducible devices via improved control of ambient conditions during fabrication. *Appl. Surf. Sci.* **2017**, *407*, 427−433.
(26) Wang, P.; Jiang, Q.; Zhao, Y.; Chen, Y.; Chu, Z.; Zhang, X.; Zhou, Y.; You, J. Synergistic improvement of perovskite film quality for efficient solar cells via multiple chloride salt additives. *Science bulletin* **2018**, *63* (11), 726−731.
(27) Cai, L.; Suen, C. W.; Lau, Y. S.; Lan, Z.; Han, J.; Zhu, F. Mitigation of morphological defects in methylammonium-free formamidinium-based perovskite solar cells. *ACS Applied Energy Materials* **2022**, *5* (7), 8304−8312.
(28) Wang, Y.; Zeng, Z.; Zhang, Y.; Zhang, Z.; Bi, L.; He, A.; Cheng, Y.; Jen, A. K. Y.; Ho, J. C.; Tsang, S. W. Unlocking the Ambient Temperature Effect on FA-Based Perovskites Crystallization by In Situ Optical Method. *Adv. Mater.* **2024**, *36* (17), 2307635.
(29) Chao, L.; Niu, T.; Gao, W.; Ran, C.; Song, L.; Chen, Y.; Huang, W. Solvent engineering of the precursor solution toward large-area production of perovskite solar cells. *Adv. Mater.* **2021**, *33* (14), 2005410.
(30) Hao, F.; Stoumpos, C. C.; Guo, P.; Zhou, N.; Marks, T. J.; Chang, R. P.; Kanatzidis, M. G. Solvent-mediated crystallization of $CH_3NH_3SnI_3$ films for heterojunction depleted perovskite solar cells. *J. Am. Chem. Soc.* **2015**, *137* (35), 11445−11452.
(31) Hamill, J. C., Jr; Schwartz, J.; Loo, Y.-L. Influence of solvent coordination on hybrid organic−inorganic perovskite formation. *ACS Energy Letters* **2018**, *3* (1), 92−97.
(32) Chung, J.; Kim, S. W.; Li, Y.; Mariam, T.; Wang, X.; Rajakaruna, M.; Saeed, M. M.; Abudulimu, A.; Shin, S. S.; Guye, K. N.; et al. Engineering Perovskite Precursor Inks for Scalable Production of High-Efficiency Perovskite Photovoltaic Modules. *Adv. Energy Mater.* **2023**, *13* (22), 2300595.
(33) Lee, D.-K.; Lim, K.-S.; Lee, J.-W.; Park, N.-G. Scalable perovskite coating via anti-solvent-free Lewis acid−base adduct engineering for efficient perovskite solar modules. *Journal of Materials Chemistry A* **2021**, *9* (5), 3018−3028.
(34) He, A.; Wang, Y.; Tang, P.; Zhang, Z.; Zeng, Z.; Zhang, Y.; Hao, X.; Wu, L.; So, S. K.; Tsang, S.-W.; Zhang, J. Unraveling the Impact of Bromine Incorporation on the Hybrid Perovskite Film Phase Evolution Mechanism by In Situ Characterization. *Adv. Energy Mater.* **2023**, *13* (39), 2300957.
(35) Zeng, Z.; Wang, Y.; Ding, S.; Li, Y.; Xiang, C.; Lee, C. S.; Cheng, Y.; Tsang, S. W. Imbalanced Surface Charge Induced Phase Segregation in Mixed Halide Perovskites. *Adv. Funct. Mater.* **2024**, 2404255.
(36) Parrott, E. S.; Patel, J. B.; Haghighirad, A.-A.; Snaith, H. J.; Johnston, M. B.; Herz, L. M. Growth modes and quantum confinement in ultrathin vapour-deposited MAPbI 3 films. *Nanoscale* **2019**, *11* (30), 14276−14284.
(37) Wagner, L.; Mundt, L. E.; Mathiazhagan, G.; Mundus, M.; Schubert, M. C.; Mastroianni, S.; Würfel, U.; Hinsch, A.; Glunz, S. W. Distinguishing crystallization stages and their influence on quantum efficiency during perovskite solar cell formation in real-time. *Sci. Rep.* **2017**, *7* (1), 14899.
(38) Shirayama, M.; Kadowaki, H.; Miyadera, T.; Sugita, T.; Tamakoshi, M.; Kato, M.; Fujiseki, T.; Murata, D.; Hara, S.; Murakami, T. N.; et al. Optical transitions in hybrid perovskite solar cells: ellipsometry, density functional theory, and quantum efficiency analyses for CH3NH3PbI3. *Phys. Rev. Appl.* **2016**, *5* (1), No. 014012.
(39) D'Innocenzo, V.; Srimath Kandada, A. R.; De Bastiani, M.; Gandini, M.; Petrozza, A. Tuning the light emission properties by band gap engineering in hybrid lead halide perovskite. *J. Am. Chem. Soc.* **2014**, *136* (51), 17730−17733.
(40) Pratap, S.; Babbe, F.; Barchi, N. S.; Yuan, Z.; Luong, T.; Haber, Z.; Song, T.-B.; Slack, J. L.; Stan, C. V.; Tamura, N.; et al. Out-of-equilibrium processes in crystallization of organic-inorganic perovskites during spin coating. *Nat. Commun.* **2021**, *12* (1), 5624.
(41) Yin, L.; Huang, W.; Fang, J.; Ding, Z.; Jin, C.; Du, Y.; Lang, L.; Yang, T.; Wang, S.; Cai, W.; et al. Crystallization Control for Ambient Printed FA-Based Lead Triiodide Perovskite Solar Cells. *Adv. Mater.* **2023**, *35* (51), 2303384.
(42) Jin, H.; Debroye, E.; Keshavarz, M.; Scheblykin, I. G.; Roeffaers, M. B.; Hofkens, J.; Steele, J. A. It's a trap! On the nature of localised states and charge trapping in lead halide perovskites. *Materials Horizons* **2020**, *7* (2), 397−410.

https://doi.org/10.1021/acsenergylett.4c03119
ACS Energy Lett. 2025, 10, 647−657